Influence of ZrB$_2$ Nanoparticles on Microstructure and Mechanical Properties of Ni-Co Coating

Yijia Wang *, Binzhou Li, Dayue Zhang [ID] **and Shanshan Si** [ID]

Ansteel Beijing Research Institute Co., Ltd., Beijing 102200, China; libz928@163.com (B.L.); zhangdayue0820@hotmail.com (D.Z.); sssupc@163.com (S.S.)
* Correspondence: wangyijiaansteel@163.com

Abstract: To improve the service life of continuous casting crystallizer, the NiCo-ZrB$_2$ coating was prepared using nanocomposite plating technology. Uniformly dispersed nano-ZrB$_2$ particles significantly enhanced the hardness and wear resistance of the coating. Upon testing, the hardness of the coating exceeded 700 HV, with a friction coefficient below 0.2, which was superior to those of pure NiCo or other nanocomposite NiCo coatings reported previously. Microscopic analysis revealed that the addition of dispersants and ultrasonic vibration treatment had facilitated the homogeneous distribution of nano-ZrB$_2$ within the matrix, thereby promoting the formation of numerous nano-twins. Due to dispersion strengthening, fine grain strengthening, and twinning strengthening, the wear behavior of the coating changed from fatigue wear to abrasive wear, and the wear volume was significantly reduced by 82%. The above findings could potentially extend the service life of the coating, reduce the cost of steel loss per ton, and have broad application prospects in other surface protection fields.

Keywords: nanocomposite plating; ZrB$_2$; nano-twins; dispersion strengthening; wear resistance

1. Introduction

At present, the protective coatings on the surface of continuous-casting crystallizer copper plates are primarily prepared using electroplating technology, with nickel–cobalt (NiCo) alloys as the primary material. During service, they face harsh working conditions such as friction and wear, alternating cold and heat, and slag-steam corrosion, making them the main loss components of the continuous casting production line. Taking the production line of Ansteel Group as an example, the pure NiCo alloy used for the copper plate of the crystallizer generally has a hardness of 300–400 HV, a steel throughput of 50,000 to 100,000 tons, and a steel loss cost of 1.5–2 CNY per ton. Enhancing the surface coating quality of crystallizer copper plates, extending their service life, and reducing the frequency of offline maintenance is of profound significance in terms of low-carbon emissions, energy conservation, environmental protection, and reducing production costs.

Nanocomposite plating technology can effectively improve the hardness and wear resistance of coatings, and it has been extensively researched both domestically and internationally. Influenced by the characteristics of industrial distribution, research and achievements related to nanocomposite plating are primarily conducted domestically, among which Liaoning University of Science and Technology, Shenyang University of Technology, China Shipbuilding Heavy Industry, and other units are active in this field. The above institutions mainly added nano-particles such as Al$_2$O$_3$ [1,2], WC [3], SiO$_2$ [4], SiC, ZrO$_2$ [5], Y$_2$O$_3$ [6], and diamond (with an addition amount of 5–15 g/L) to the plating solution, utilizing ultrasonic treatment to disperse the aggregated nanoparticles through mechanical vibration [7–14]. After electroplating, the hardness of the composite coatings ranged from 300 to 500 HV, and the friction coefficient was between 0.4 and 0.5.

However, there are still some concerns that need to be addressed in the process. Firstly, after being dispersed by ultrasound, nanoparticles still tended to aggregate and settle.

Ultrasound alone was not sufficient to form a uniform suspension, and its dispersion effect gradually decreased with the prolongation of ultrasound time. Most of the added nanoparticles did not participate in the reaction, resulting in waste. Secondly, the surface properties of different nanoparticles varied, and their wettability with nickel-based materials was poor. Without surface modification, it was sometimes difficult to integrate with nickel-based coatings, which could lead to agglomeration, poor dispersion effect, abnormal grain growth, and affected coating quality. Thirdly, due to the limitations of intrinsic strength and hardness, oxide-dispersed phases cannot further improve the performance of coatings. At the same time, its lower thermal conductivity has a negative impact on coatings serving at high temperatures.

In ultra-high temperature ceramics field, ZrB_2 is unique. It has higher hardness, strength, melting point, and thermal conductivity than traditional carbides and oxides. The strengthening research of borides in NiCo alloys is rarely studied. To this end, this work creatively selected ZrB_2 as the strengthening phase. By adding an appropriate amount of dispersant, the surface of nano-ZrB_2 particles was modified to promote uniform dispersion and achieve co-deposition with the NiCo matrix. After successfully preparing NiCo-ZrB_2 samples, in-depth characterization and analysis were conducted on their microstructure, hardness, and wear resistance while the strengthening mechanism was further discussed.

2. Materials and Methods

2.1. Construction of Nanocomposite Plating Device

The nanocomposite plating device constructed in this study is shown in Figure 1, which consisted of a multi-channel electrochemical workstation (Manufacturer: Wuhan Blue Electric Electronics Co., Ltd., Wuhan, China), a mechanical stirrer, an ultrasonic generator, a sample fixing table, an electroplating tank, and other parts. It could apply coupling field effects to the workpiece and plating solution, including current, heating, stirring, and ultrasonic oscillation.

Figure 1. Photo of nanocomposite plating device.

2.2. Composition of Nanocomposite Plating Solution

The composition of the nanocomposite plating solution designed in this work is presented in Table 1. All chemical agents were sourced from China National Pharmaceutical Group Chemical Reagent Co., Ltd., Shanghai, China. Nickel aminosulfonate and cobalt aminosulfonate were the primary salts. By adjusting the ratio of nickel salt to cobalt salt, the nickel cobalt content ratio was achieved at 5:1. Sodium dodecyl sulfate and polyvinylpyrrolidone served as surface modification and dispersion, which was the key to solving the dispersion and suspension of nanoparticles. ZrB_2 particles were in the strengthening phase, with an average particle size of 50 nm (Source: Shanghai Maoguo

Nano Technology Co., Ltd., Shanghai, China). Boric acid acted as a buffering agent to ensure that the solution remained acidic and maintained a stable pH throughout the electroplating process.

Table 1. Composition of nanocomposite plating solution.

Component	Nickel Sulfamate	Cobalt Sulfamate	Sodium Dodecyl Sulfate	Polyvinyl Pyrrolidone	ZrB$_2$	Boric Acid
Function	Nickel salt	Cobalt salt	Surface modifier	Surface dispersant	Strengthening particles	Control the pH
Content	50–100 g/L	5–20 g/L	-	-	0–5 g/L	30–60 g/L

Configuration process:

(1) Firstly, the primary salt and dispersant were separately weighed and placed into the electroplating tank. (2) Secondly, deionized water was added to the tank and then heated to 40 °C. Boric acid was added and stirred until the solution was clarified. (3) Thirdly, nanoparticles were added into the tank while initiating ultrasonic treatment for 30 min to complete the plating solution preparation.

2.3. Sample Preparation

Two samples were prepared: sample A (with dispersant added) and sample B (without dispersant added). Sample B was prepared without adding sodium dodecyl sulfate and polyvinylpyrrolidone to the plating solution to verify the effect of the dispersant. The other parameters were identical for both samples. The range of electroplating process parameters is presented in Table 2.

Table 2. Process parameters of nanocomposite plating.

Temperature of Plating Solution	Ultrasonic Power	Stirring Rate	Current Density	Electroplating Time
40–60 °C	0–300 W	0–300 r/min	3–6 A/dm^2	1–10 h

Preparation process: (1) Two copper plates were cut into $25 \times 50 \times 5$ mm^3 from the narrow edge copper plate surface of the crystallizer as the cathode. The anode was composed of high-purity nickel plate. (2) The copper plate surface was uniformly coated with 704 corrosion-resistant silicone to cover non-plating areas and allowed it to cure for later use (curing time: 3 h). (3) The copper plate surface intended for plating was ground with sandpaper with grit sizes ranging from 400 to 1200. After that, it was cleaned with deionized water and alcohol and, finally, immersed in a 10% hydrochloric acid solution for activation. (4) The cathode plate and anode plate were connected to the power supply and fixed with clamps, then placed into the solution. (5) Starting stirring, ultrasonication, and heating treatment, when the temperature reached the preset value, started electroplating for 5 h.

2.4. Testing and Analysis Methods

(1) The original coatings were investigated by a scanning electron microscope (Thermo Fisher Axia ChemiSEM, Waltham, MA, USA). The surface morphology and roughness of the coating were measured by atomic force microscopy (AFM, Park System Corp., KOR, Suwon, Republic of Korea). The fine structure and second-phase particles inside the coating were observed and analyzed by a transmission electron microscope (TEM, Tencnai F20, Thermo Fisher, Waltham, MA, USA).

(2) The hardness of the coatings was measured using a Vickers microhardness tester, with a diamond indenter in the shape of a pyramid, a load set at 200 g, and a holding time of 15 s. We measured each sample 5 times and took the arithmetic mean of the 5 test data.

(3)　The friction coefficient and wear volume of coating were measured using a reciprocating sliding friction and wear tester. Sample size: $8 \times 15 \times 5.5$ mm^3. Test temperature: room temperature. Load: 1 N. Frequency: 10 Hz. Journey: 5 mm. Dry friction using 10 mm GCr ball. Friction time: 1 min.

3. Results and Discussion

3.1. Sample Morphology Analysis

As shown in Figure 2, both samples A and B had a silver-gray NiCo coating fully covering the reddish-brown copper substrate. There were no defects such as pinholes, bubbles, peeling, burning, or delamination, proving that the composite plating device and plating solution were functioning well, and the electroplating parameters were set reasonably.
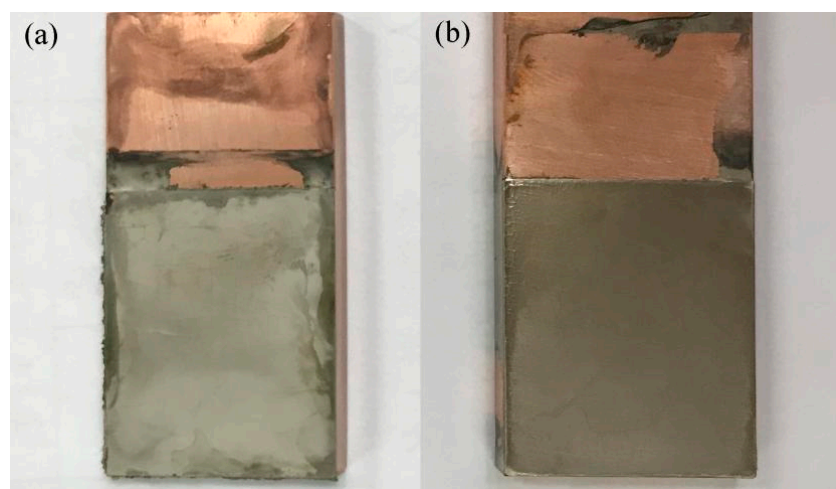

Figure 2. Nanocomposite plating sample (**a**) with dispersant added sample (**b**) without dispersant added sample.

As shown in Figure 3a,a', the surface of sample A was relatively rough, featuring a spherical NiCo alloy morphology with diameters ranging from 0.40 to 2.49 μm. A large number of sheet-like and granular second-phase particles were embedded, with an average size of 0.51 μm. As shown in Figure 3b,b', the surface of sample B was relatively smooth, featuring only a small amount of spherical morphology with diameters ranging from 0.38 to 7.86 μm. Only a small number of second-phase particles, with an average size of 0.47 μm, were embedded on the surface of sample B. Energy dispersive spectroscopy (EDS) analysis was performed on the second-phase particles at the red circle position, and significant peaks of Zr and B elements were detected in addition to matrix elements such as Ni and Co, suggesting that the above particles should be ZrB$_2$. From this, it could be seen that compared to sample B, sample A had more ZrB$_2$ particles embedded and distributed on its surface, significantly changing the morphology of the coating. To quantify this change, AFM testing was performed on two samples. As shown in Figure 3c,d, the AFM test results showed the local three-dimensional morphology of the surfaces of two samples. After measurement, the surface roughness Sq of sample A was 62.7 nm, while that of sample B was 41.3 nm. The higher roughness of sample A was consistent with the SEM results.

To verify whether nanoparticles were only enriched on the surface, the side of sample A was polished, and the cross-section of the coating was observed. In Figure 4a, it was evident that the coating was flat and uniform, tightly bonded to the substrate, with a thickness of 165 μm (deposition rate was about 30 μm/h). As shown in Figure 4c,d, after erosion, obvious particles could be observed in the internal area of the cross-section at high magnification. EDS results demonstrated the presence of significant Zr element peaks, indicating uniform particle distribution inside the coating. A portion of the coating was peeled off and a fracture surface was created, as illustrated in Figure 4b. The cross-section

had uniform longitudinal patterns with columnar crystal features, indicating that the coating grew layer by layer along the direction perpendicular to the substrate.
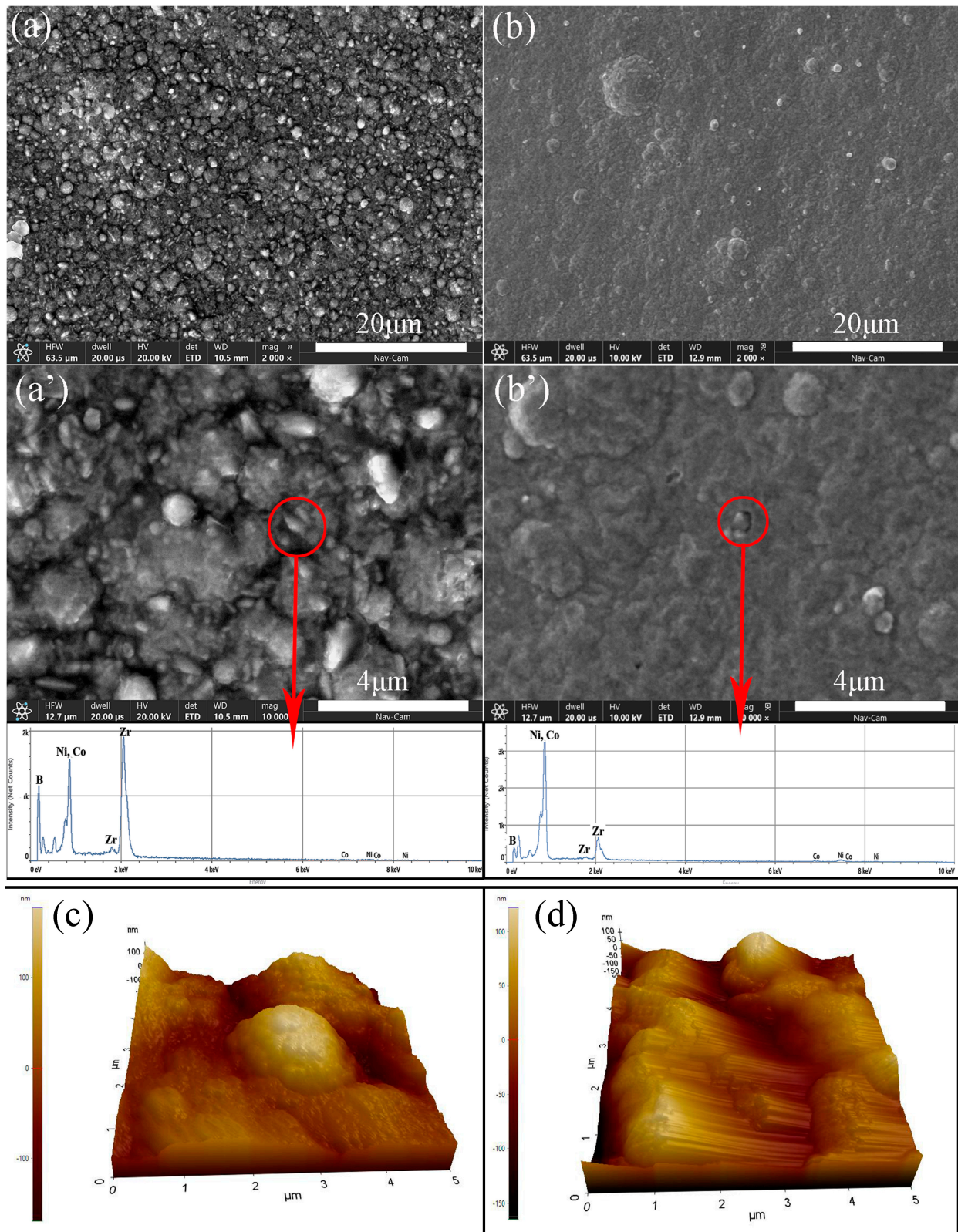

Figure 3. Sample surface micrograph and energy spectrum test results, (**a**,**a'**) sample A, (**b**,**b'**) sample B, (**c**) AFM surface morphology characteristics of sample A, (**d**) AFM surface morphology characteristics of sample B.
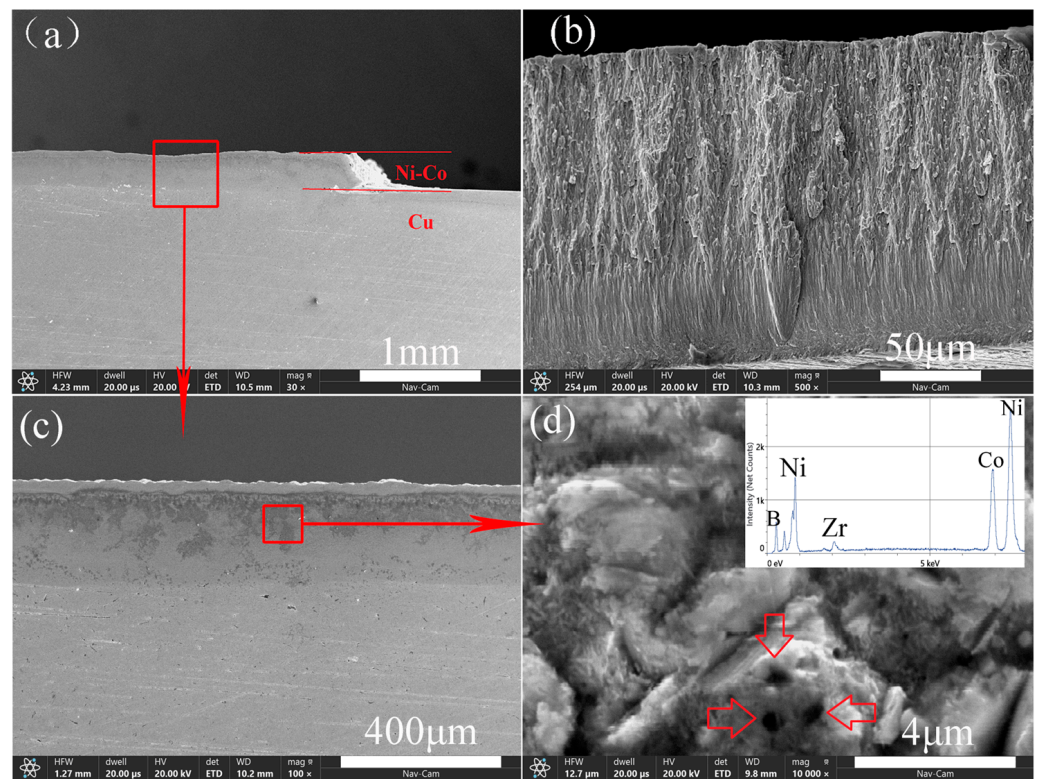
Figure 4. Coating micrograph (**a**) surface, (**b**) cross-section, (**c**,**d**) section selection and energy spectrum test results after polishing erosion.

Comparing the surface morphology of samples A and B, the morphological differences between the two samples were related to the dispersion degree of the nanoparticles. The nanoparticles added to the plating solution had high specific surface area and surface energy, which were prone to agglomerate and form large particles, settling with the flow of the plating solution and failing to effectively deposit within sample B. For sample A, when the ultrasonic oscillation opened up the aggregation of nanoparticles, the long-chain molecules of the dispersant adsorbed onto the particle surface, creating steric hindrance and electrostatic repulsion effects, avoiding secondary aggregation of particles, forming a uniform suspension, allowing more nanoparticles to adsorb onto the substrate surface. During electroplating, due to the heterogeneous nucleation effect, the nanoparticles on the substrate surface served as nucleation backbones of the NiCo alloy, preferentially enveloping the nucleation on the particle surface, gradually growing and forming a spherical morphology. The higher the dispersion degree of the particles, the more prominent the spherical morphology became.

3.2. Sample Performance Analysis

The Vickers microhardness and friction performance of two samples were tested and compared with literature reports, with the results presented in Table 3.

Table 3. Performance of nanocomposite plating samples.

Sample	Hardness (HV)	Coefficient of Friction	Wear Volume
Pure-NiCo/NiCo-Al$_2$O$_3$ [1]	325/360	-	-
NiCo-Al$_2$O$_3$ [2]	415	0.39	-
Pure-NiCO/NiCo-WC [3]	416/467	-	-
Pure-NiCo/NiCo-SiO$_2$ [4]	470/480	0.41/0.42	
Sample B	493 ± 14	0.363	7.88×10^{-3}/mm^3
Sample A	713 ± 22	0.14	1.42×10^{-3}/mm^3

3.2.1. Hardness Analysis

According to literature reports and practical experience in continuous casting production lines, the hardness of pure NiCo alloy typically ranges between 350 and 400 HV. It could be observed that doping with nanoparticles such as Al_2O_3, SiO_2, WC, and ZrB_2 could enhance the hardness of Ni-Co coatings. Taking the data in the first, third, and fourth rows of Table 3 as an example, compared to pure NiCo alloy, the addition of nanoparticles increased the hardness of the samples by 10.7%, 12.2%, and 2.1%, respectively. Sample A prepared in this study exhibited a hardness of 713 HV, significantly higher than NiCo alloy (with and without nanoparticles) reported in the literature, indicating that ZrB_2 particles provided superior reinforcement effects. Meanwhile, the hardness of sample A increased by 44% compared to sample B, indicating that a more uniform particle distribution results in a higher reinforcement effect.

3.2.2. Friction Analysis

The surface morphology of samples A and B before and after friction was shown in Figure 5a,b. A clear scratch appeared in the middle area of both samples. The scratch width of sample A was smaller than that of sample B. The friction curves of the two samples are shown in Figure 5c,d. It could be seen that when the friction distance reached 100 mm, sample A entered the stable friction stage, and the curve was smooth without significant fluctuations, with an average friction coefficient of 0.14. For sample B, when the friction distance reached 150 mm, it entered the stable friction stage. Subsequently, as the friction distance increased, the friction coefficient slowly rose and significantly increased after 380 mm, with significant fluctuations. The average friction coefficient was 0.363. The wear volume of sample A was only 18% of that of sample B, while its friction coefficient was lower than reported in the literature.
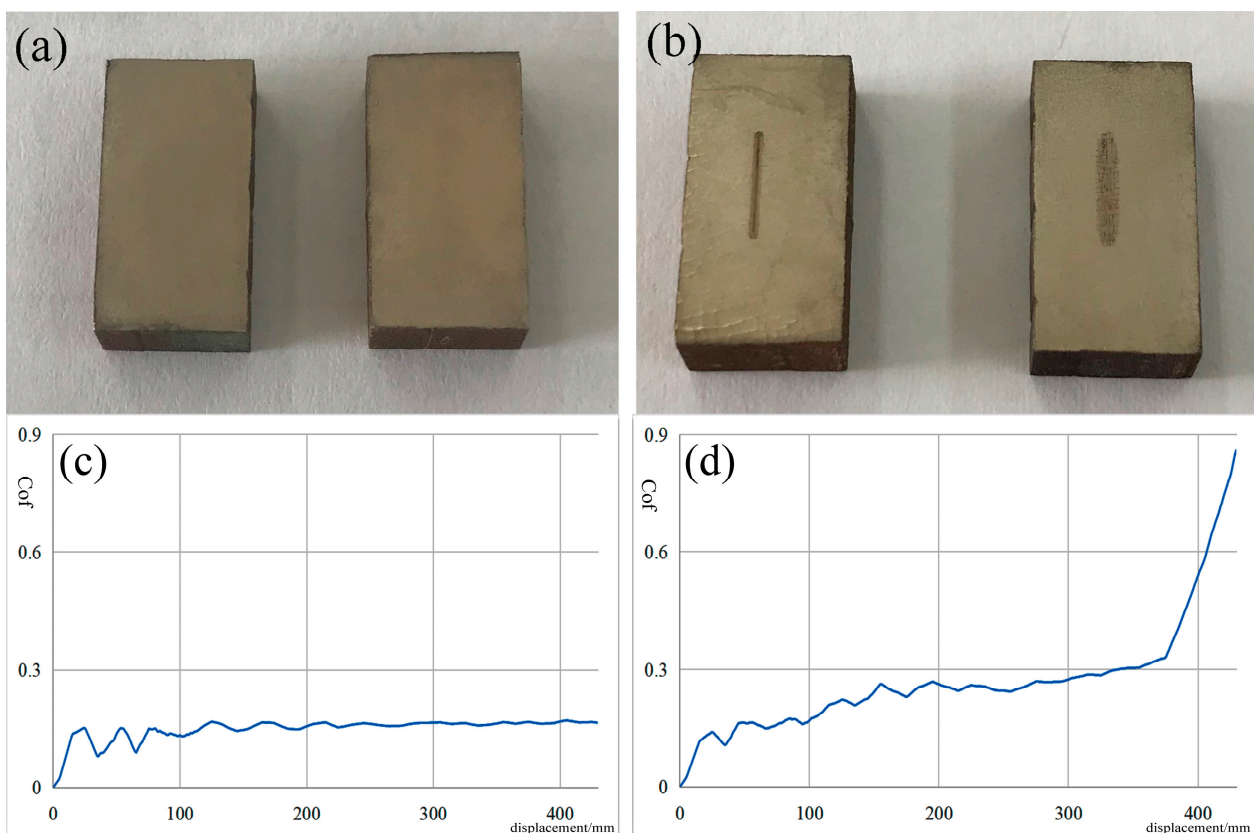

Figure 5. Friction and wear test sample surfaces (**a**) before testing, (**b**) after testing, (**c**) friction curve of sample A, (**d**) friction curve of sample B.

Friction performance is closely related to wear mechanism. As shown in Figure 6, the friction areas of samples A and B were observed under SEM. Sample A had a relatively flat surface with small parallel plow groove-shaped wear marks, which were speculated to be brought about by a large number of ZrB_2 particles embedded on the surface during compression and reciprocating motion. The damage mechanism was abrasive wear. In contrast, the surface of sample B was relatively rough, with numerous pits and irregular flake-like spalling traces. It was speculated that fatigue occurred in the contact area under cyclic stress, leading to the peeling of the surface material. The damage mechanism was fatigue wear. From this, it could be concluded that more ZrB_2 in sample A helped to improve the fatigue strength of the material, changed the wear behavior, reduced the wear amount, and extended the service life of the composite coating.
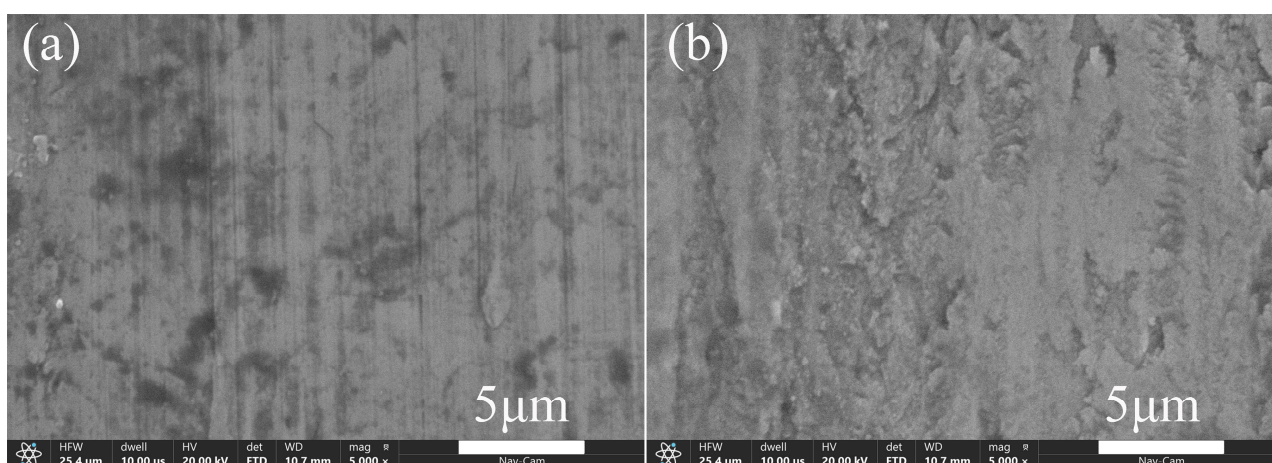

Figure 6. Surface scratches (**a**) sample A, (**b**) sample B.

3.3. Strengthening Mechanism Analysis

Based on the above results, it was evident that sample A exhibited better wear resistance. To delve deeper into its underlying strengthening mechanisms, transmission electron microscope (TEM) observations and analyses were conducted on typical regions within Sample A, with the results being presented in Figure 7.

In the field of view shown in Figure 7a, a large number of spherical particles were dispersed throughout the matrix, with an average size of 3.91 nm and an average spacing of 9.06 nm. In Figure 7b, there were not only small spherical particles but also ellipsoidal particles with a size greater than 200 nm. Energy dispersive spectroscopy (EDS) mapping analysis of the selected area in Figure 7(a1) and the ellipsoidal particles in Figure 7b revealed enrichment regions of B and Zr elements that coincided with the morphological distribution of the spherical particles. Diffraction analysis was performed on ellipsoidal particles (as shown in Figure 7(b1)), and Fourier transform analysis indicated that the interplanar spacing (OA-2.82 Å, OB-2.17 Å) and angle (∠AOB-113°) were consistent with the (0, 1, 0) and (1, −1, −1) planes of ZrB_2, proving that both types of particles were ZrB_2.

Further observation of the matrix revealed that the grains had equiaxed characteristics with an average size of approximately 64 nm due to the TEM sample preparation direction being perpendicular to the growth direction. As shown in Figure 7a,c, a large number of parallel band structures with an average width of 6.87 nm were distributed within these grains and had symmetrical relationships, which was a typical feature of twin crystals. Diffraction analysis was conducted on the band region, as shown in Figure 7d. It could be seen that the diffraction pattern exhibited the characteristic of symmetry along the (1, −1, −1) plane, which was consistent with the twinning characteristics of FCC metals, proving the generation of a large number of nano-nickel twins in the matrix. A high-resolution photograph of the nano-twin region was shown in Figure 8a, where Area-1 represented nano-ZrB_2 particles, the area between concentric circles represented the interface between ZrB_2 and

the matrix, and Area-2 represented the interior of the twin. The inverse Fourier transform analysis was performed on Area-1 and -2, with the results presented in Figure 8b,c. At the interface between ZrB_2 particles and matrix, significant lattice distortion occurred, with obvious dislocation pile-up and stress concentration phenomena. Inside the twins, multiple half-atomic planes could be observed, indicating the presence of numerous edge dislocations (marked with "T" in Figure 8a). Owing to the presence of ZrB_2 particles, there were differences in the growth rate of the local matrix, resulting in increased internal stress. In order to relieve stress, the matrix underwent twinning deformation, forming a large number of nano-twins.
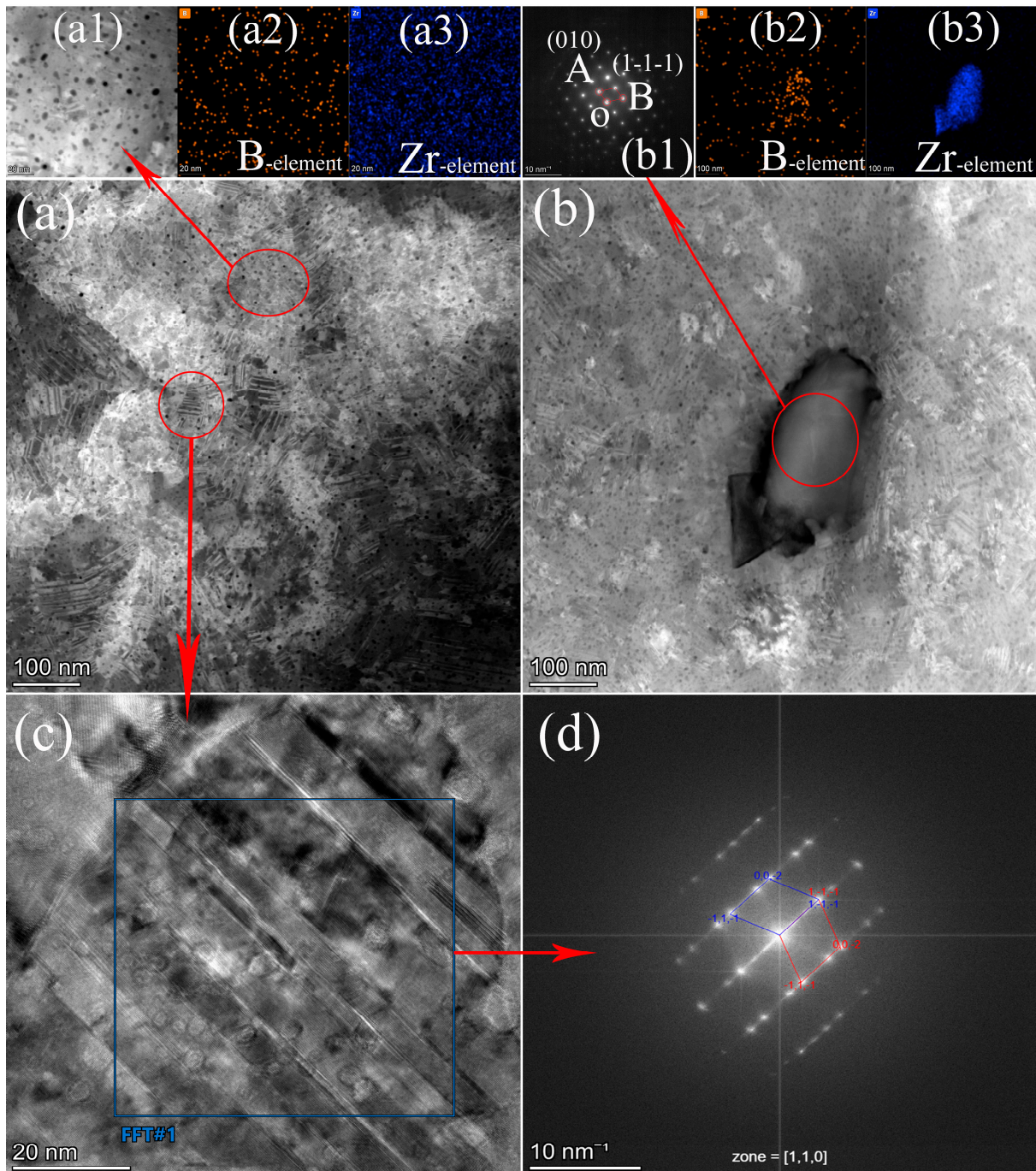
Figure 7. Sample A transmission electron microscopy images (**a**,**b**) of typical internal regions, (**c**,**d**) selection and diffraction images of nanocrystals, (**a1**–**a3**) selected area energy spectrum scanning results, (**b1**–**b3**) selected area diffraction and energy spectrum scanning results.
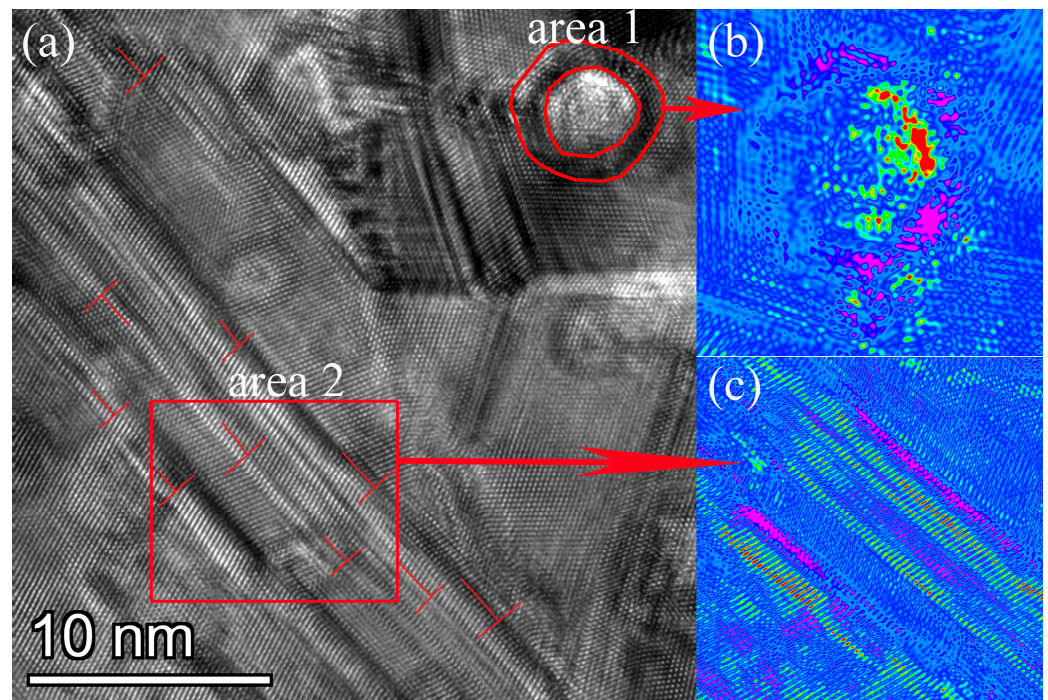
Figure 8. (**a**) High-resolution photos of nano-twin crystals, (**b,c**) selected area inverse Fourier transform processed photos.

The fine and uniformly dispersed ZrB_2 particles significantly inhibited the growth of the matrix grains. According to the Hall Petch effect (Equation (1), as the grain size (d) of the material decreased, its strength (σ_s) increased. As described in the literature [15–18], when the grain sizes of nickel, copper, and steel reached the nanoscale, their hardness and structural stability were significantly enhanced, leading to improved wear resistance and fatigue performance. Additionally, based on the Taylor model (Equation (2)), an increase in dislocation density (ρ) led to an increase in strength (τ_c). When the alloy underwent deformation under external loads, movable dislocations encountered ZrB_2 particles and twin boundaries, which hindered the movement of dislocations and significantly increased the dislocation density in local regions, promoting the formation of dislocation grids and entanglement. As described in the literature [19], the interaction between dislocations and high-density twin boundaries resulted in the formation of numerous dislocations. These dislocations then glided, accumulated, and proliferated along the twin boundaries, contributing to work hardening and accommodating plastic deformation, thereby enhancing overall mechanical properties. Furthermore, according to the literature [20], twin boundaries were less prone to initiate fatigue cracks compared to conventional grain boundaries. This was primarily attributed to the reduction in Schmid factor differences, the increase in stacking fault energy, and the change in slip mode. Twin boundaries allowed for more dislocations to pass through, significantly increasing the resistance to fatigue crack initiation. Based on dispersion strengthening and twin strengthening effects, sample A exhibited higher hardness, a lower friction coefficient, and a reduced wear volume.

$$\sigma_s = \sigma_0 + kd^{-1/2} \tag{1}$$

$$\tau_c = \alpha b G \sqrt{\rho} \tag{2}$$

4. Conclusions

(1) Adding sodium dodecyl sulfate and polyvinylpyrrolidone to the plating solution could effectively modify the surface of nano-ZrB_2 particles, promote the co-deposition

of nanoparticles and NiCo alloy, and achieve uniform dispersion of ZrB$_2$ particles inside the NiCo coating.

(2) Uniformly dispersed nano-ZrB$_2$ particles could promote the formation of a large number of nano-twins in the matrix. Under the effects of dispersion strengthening and twin strengthening, the hardness of the coating significantly increased to over 700 HV, which was higher than similar coatings reported in the literature.

(3) The uniformly dispersed ZrB$_2$ particles and nano-twins caused the wear mechanism of the samples to shift from fatigue wear to abrasive wear, resulting in a friction coefficient below 0.2 and a substantial reduction in wear volume.

The above findings provided a good reference for the field of surface protection. Further performance testing under high temperature and corrosion conditions is needed in the future to lay a solid foundation for the practical application of the coatings.

References

1. Wang, Y.Y.; Su, J.M.; Han, C.F.; Jin, H.; Zhang, J.W.; Song, H.; Li, J. Study of preparation of Ni-Co-Al$_2$O$_3$ Nanocomposite coating by electro-deposition. *Nonferrous Met.* **2015**, *2*, 53–57. [CrossRef]
2. Yao, J.H.; Ye, L.W.; Luo, F.; Zhang, W.; Kong, F.Z.; Dong, S.Y. Laser strengthening nano-composite plating Al$_2$O$_3$ coating. *Chin. J. Lasers* **2007**, *34*, 998–1003.
3. Yang, H.L. Optimization of process conditions for electrodeposition of Ni-Co/WC composite coatings on red copper from sulfate bath. *Plat. Finish.* **2021**, *43*, 5.
4. Bai, S.F.; Liu, X.H.; Xu, L.K.; Xuan, J.J.; Shao, Y.; Xin, Y.L.; Li, X.; Fan, L. Effect of SiO$_2$ particles size on properties of Ni-Co-SiO$_2$ electrodeposited composite coatings. *Dev. Appl. Mater.* **2021**, *36*, 12–20. [CrossRef]
5. Wang, Y.Y.; Zhou, X.Y.; Liang, Z.P.; Jin, H. Characterization of Ultrasonic-Assisted Electrochemical Deposition of Ni-Co-ZrO$_2$. *Coatings* **2018**, *8*, 211. [CrossRef]
6. Xing, S.L.; Wang, L.B.; Jiang, C.H.; Liu, H.B.; Zhu, W.L.; Vincent, J. Influence of Y$_2$O$_3$ nanoparticles on microstructures and properties of electrodeposited Ni–W–Y$_2$O$_3$ nanocrystalline coatings. *Vacuum* **2020**, *181*, 109665. [CrossRef]
7. Cai, F.; Cai, X.J.; Zhang, S.H.; Jiang, C.H. Microstructure evolution and improved corrosion resistance of electrodeposited NiCo-Al composite coatings with different Al contents. *J. Alloy Compd.* **2018**, *738*, 72–78. [CrossRef]
8. Sadeghi, A. *Microstructure Evolution and Strengthening Mechanism in Ni-Based Composite Coatings*; Technische Universität Chemnitz: Chemnitz, Germany, 2016.
9. Liu, Y.; Yu, S.R.; Liu, J.D.; Han, Z.W.; Yuan, D.S. Microstructure and wear resistance of electrodeposited Ni-SiO$_2$ nano-composite coatings on AZ91HP magnesium alloy substrate. *Trans. Nonferr. Metal Soc.* **2011**, *21*, s483–s488. [CrossRef]
10. Cui, L.F.; Li, X.; Li, C.Y.; Zhu, L.J.; Zhang, Q.G.; Li, Z.; Liu, H.Y. Research on the Corrosion Resistance of Electrodeposited Ni-SiC Composites Constructed for Steel Storage Tank Application. *Materials* **2024**, *17*, 4616. [CrossRef] [PubMed]
11. Guerguer, L.; Hamdi, A.; Ziouche, A.B.A. Influence of surfactant concentration on structural properties and corrosion behaviour of electrodeposited Ni-SiO$_2$ nanocomposite coatings. *Int. J. Mater. Res.* **2023**, *114*, 175–190. [CrossRef]
12. Ma, C.Y.; Li, H.X.; Xia, F.; Xiao, Z. Effect of Ultrasonic Power on Microstructure and Properties of Ultrasonic-Assisted Electrodeposited Ni–Al$_2$O$_3$ Thin Nanocoatings. *Trans. Indian Inst. Met.* **2022**, *75*, 1669–1679. [CrossRef]
13. Bai, S.; Liu, X.; Xu, L.; Xuan, J.; Liu, Y.; Shao, Y.; Xin, Y.; Li, X.; Fan, L. Enhancement of corrosion resistance and lubricating performance of electrodeposited Ni-Co coating composited with mesoporous silica nanoparticles and silicone oil impregnation. *Mater. Chem. Phys.* **2022**, *282*, 125929. [CrossRef]
14. Long, X.; Hang, T.; Guo, Y.; Li, Y.; Wu, Y.; Ling, H.; Hu, A.; Li, M. Influence of intercolony boundary on corrosion behavior of electrodeposited Ni–W alloy for electronic connector applications. *Mater. Chem. Phys.* **2020**, *239*, 121989. [CrossRef]

15. Liu, X.C.; Zhang, H.W.; Lu, K. Strain-Induced Ultrahard and Ultrastable Nanolaminated Structure in Nickel. *Science* **2013**, *342*, 337–340. [CrossRef] [PubMed]

16. Lu, L.; Shen, Y.F.; Chen, X.H.; Qian, L.H.; Lu, K. Ultrahigh strength and high electrical conductivity in copper. *Science* **2004**, *304*, 422–426. [CrossRef] [PubMed]

17. Fang, T.H.; Li, W.L.; Tao, N.R.; Lu, K. Revealing extraordinary intrinsic tensile plasticity in gradient nano-grained copper. *Science* **2011**, *331*, 1587–1590. [CrossRef] [PubMed]

18. Lu, K.; Yan, F.K.; Wang, H.T.; Tao, N.R. Strengthening austenitic steels by using nanotwinned austenitic grains. *Scr. Mater.* **2012**, *66*, 878–883. [CrossRef]

19. Li, X.Y.; Wei, Y.J.; Lu, L.; Lu, K.; Gao, H.J. Dislocation nucleation governed softening and maximum strength in nano-twinned metals. *Nature* **2010**, *464*, 877–880. [CrossRef] [PubMed]

20. Lu, K.; Lu, L.; Suresh, S. Strengthening materials by engineering coherent internal boundaries at the nanoscale. Science. *Science* **2009**, *324*, 349–352. [CrossRef] [PubMed]